Isotope effects on the ionization of hydrogen molecular ions in strong laser fields

Liang Xu,[1] Chen-Xi Hu,[1,2] and Feng He[1,3,*]

[1]*Key Laboratory for Laser Plasmas, Ministry of Education, and School of Physics and Astronomy, Shanghai Jiao Tong University, Shanghai 200240, China*

[2]*Zhiyuan Innovative Research Center, Shanghai Jiao Tong University, Shanghai 200240, China*

[3]*Collaborative Innovation Center of IFSA, Shanghai Jiao Tong University, Shanghai 200240, China*

(Received 13 December 2018; revised manuscript received 2 February 2019; published 25 March 2019)

Isotope effects on the ionization of hydrogen molecular ions in strong laser fields are studied by numerically simulating the time-dependent Schrödinger equation. Though the isotopes of hydrogen molecular ions have identical Born-Oppenheimer potential curves, the distinct ionization scenarios are observed for single-photon, multiphoton, and tunneling ionization. For multiphoton and tunneling ionization, the ionization rate of H_2^+ is larger than that of D_2^+ and T_2^+. The ratio of the intensity-dependent tunneling ionization probabilities of H_2^+ (D_2^+) and T_2^+ can be qualitatively explained by the adiabatic tunneling theories if a few-femtosecond ultrashort pulse is used. For tens of femtosecond laser pulses, the nuclear movement is unavoidable and the time-dependent Schrödinger equation simulation is necessary in order to calculate the ionization probability accurately. For single-photon ionization, the electron-nuclei joint energy spectra are distinct though the total ionization probabilities are similar. The elastic constant of potential curves can be retrieved by comparing the single-photon-induced electron-nuclei joint energy spectra of different isotopic molecular ions, which offers a potential technique to image molecules.

DOI: 10.1103/PhysRevA.99.033420

I. INTRODUCTION

As the simplest molecule in nature, H_2^+ and its isotopic molecules serve as important prototypes for understanding the ultrafast dynamics in molecules [1–3]. Among all the ultrafast phenomena, ionization and dissociation are overwhelmingly important and have attracted a great deal of attention [4,5]. For dissociation, several mechanisms have been explored, such as bond softening [6], bond hardening [7], and above-threshold dissociation [8,9]. During dissociation, the behavior of the unique electron in the system can be controlled by external fields. The isotope effect plays an important role in the electron localization during the dissociation of hydrogen molecular ions. For H_2^+, D_2^+, and T_2^+, the nuclei will spend different times reaching the critical internuclear distance, where laser-induced resonant coupling between the $1s\sigma_g$ and $2p\sigma_u$ states occurs. Therefore, the isotopical hydrogen molecular ions will see a different phase of the steering laser field when the resonant coupling happens, which results in different electron localization for different isotopical molecules [10–12]. The nuclear wave packets also have distinct collapse and revival times for H_2^+, D_2^+, and T_2^+ ions [13,14].

It is accepted that the isotope effects play important roles in molecular dissociation. Similarly, in the dissociative ionization of hydrogen molecules, the isotope effects are also believed to be important. Due to the different relaxation of molecular bonds with different nuclear masses, high harmonic generation (HHG) has different efficiencies in H_2 and D_2 [15–17]. For heteronuclear molecular ions such as HT^+, the asymmetric movement of the two nuclei may also produce different HHG when the carrier envelope phase (CEP) of the driving laser field shifts by π [18]. The isotope effects should also be important in the redshift and blueshift of the HHG [19] and in increasing HHG efficiency and extending cutoff simultaneously by using chirped driving pulses [20].

In contrast, for the ionization of molecules, it is believed that the nuclei are frozen during the release of the electron and thus the fixed-nuclei approximation is widely adopted [21–23]. Such an approximation is reasonable since the electron inertia and nucleus inertia differ by three orders of magnitude. The fixed-nuclei approximation greatly simplifies the theoretical study of molecules in strong laser fields since the electron dynamics and nuclear dynamics can be separated from each other. According to the fixed-nuclei approximation, H_2, D_2, and T_2 are expected to have the same ionization probabilities since they have identical Born-Oppenheimer potential curves. However, recently, Tolstikhin *et al.* predicted theoretically that H_2 should be more easily ionized than the other two isotopic molecules in the adiabatic tunneling ionization [24–26]. Such a prediction has been confirmed in experiment by Wang *et al.* by measuring the ionization probabilities using mixed H_2 and D_2 gases [27]. The different nuclear movements of isotopic molecules during the ionization were suggested to explain the physics behind the observation.

In this paper we numerically study the electron-nuclear joint energy spectra (JESs) in the single-photon, multiphoton, and tunneling ionization of the hydrogen molecular ion and its isotopic molecular ions in strong laser fields. In single-photon ionization, compared to H_2^+, the ionization fragments of T_2^+ have a larger proportion of higher-nuclear-energy components but a lower proportion of lower-nuclear-energy components,

*fhe@sjtu.edu.cn

whereas the total ionization probabilities of H_2^+ and T_2^+ are similar. In tunneling ionization, the ionization rate of H_2^+ is larger than that of T_2^+ (D_2^+) and the ratio of the ionization probabilities of H_2^+ (D_2^+) and T_2^+ decreases monotonically with an increase of the laser intensity. We compare the results of the time-dependent Schrödinger equation (TDSE) and the established tunneling theories over a wide range of laser parameters. The influence of the nuclear motion on ionization probability is also studied systematically.

The rest of the paper is organized as follows. In Sec. II we present the details of the numerical method. Section III discusses the electron-nuclear JESs of the single-photon ionization (Sec. IIIA), multiphoton ionization (Sec. IIIB), and tunneling ionization (Sec. IIIC). A summary is provided in Sec. IV.

II. NUMERICAL METHODS

To preserve the coherence of electron and nuclei during the ultrafast ionization, we numerically simulate the TDSE by treating nuclear and electronic motions on equal footing (atomic units are used unless stated otherwise)

$$i\frac{\partial}{\partial t}\psi(z,R;t) = [H_0 + V_L(z,t)]\psi(z,R;t), \tag{1}$$

where H_0 is the field-free Hamiltonian

$$H_0 = \frac{p_R^2}{2M} + \frac{p_z^2}{2m} + V(z,R). \tag{2}$$

In Eq. (2), R and z are the internuclear distance and electronic displacement, respectively, p_R and p_z are the nuclear and electronic momentum operators, respectively, and $M = M_n/2$ and $m = 2M_n/(2M_n+1)$ are the reduced nuclear and electronic mass, respectively, where M_n is the nuclear mass of the homonuclear diatomic molecule. Such a reduced-dimensionality model is able to capture the main picture qualitatively since the electron wave-packet expansion perpendicular to the molecular axis does not result in extra dynamics. To better reproduce the molecular potential curves, the Coulomb potential $V(z,R)$ is written as

$$V(z,R) = \frac{1}{R} - \frac{1}{\sqrt{(z+R/2)^2 + \left(\frac{\beta(R)}{5}\right)^2} + \frac{1}{\beta(R)} - \frac{\beta(R)}{5}} - \frac{1}{\sqrt{(z-R/2)^2 + \left(\frac{\beta(R)}{5}\right)^2} + \frac{1}{\beta(R)} - \frac{\beta(R)}{5}}, \tag{3}$$

where $\beta(R)$ is the R-dependent soft-core parameter [28]. By choosing proper $\beta(R)$, not only is the $1s\sigma_g$ potential curve accurately produced, but also the $2p\sigma_u$ potential curve is comparable to the real case. After the initial state is obtained in the imaginary-time propagation [29], we propagate the wave function in real time using the Crank-Nicolson method [30]. The laser-electron interaction is expressed in the dipole approximation

$$V_L(z,R;t) = zE(t). \tag{4}$$

The linearly polarized laser field is described as $E(t) = E_0\sin^2(\pi t/\tau)\sin(\omega t+\phi)$. The laser parameters, such as the intensity I (or the amplitude E_0), the frequency ω, the pulse duration τ, and the CEP ϕ, are variable in the following simulations. The spatial and time steps are $\Delta R = 0.02$ a.u., $\Delta z = 0.05$ a.u., and $\Delta t = 0.1$ a.u. The $R \times z$ two-dimensional simulation box is sampled by $800 \times 40\,000$ grids, which is big enough to keep the entire ionized wave packet. Therefore, no absorbers in boundaries are necessary. The convergence of the calculations is tested by using finer spatial and time grids whereby almost identical results are obtained.

After the laser-molecule interaction, we use the resolvent technique to calculate the electron-nuclear JES [31–33]. By applying the electronic and nuclear resolvent operators successively to the wave function at the terminal time t_f, we obtain a temporary function

$$|\Psi'\rangle = R^n_{\epsilon_\mu}(E_\mu)R^n_{\epsilon_e}(E_e)|\Psi(t_f)\rangle, \tag{5}$$

from which the differential probability density ρ with the asymptotic kinetic energies E_e and E_μ is given as

$$\rho(E_e,E_\mu) = \frac{\langle\Psi'|\Psi'\rangle}{\alpha_e\alpha_\mu}, \tag{6}$$

where the denominators $\alpha_e = \epsilon_e\frac{\pi}{n}\csc(\frac{\pi}{2n})$ and $\alpha_\mu = \epsilon_\mu\frac{\pi}{n}\csc(\frac{\pi}{2n})$. Here ϵ_e^n and ϵ_μ^n are the electronic and nuclear energy resolutions, respectively. In the following calculations, $n = 2$, $\epsilon_\mu^n = 0.02$, and ϵ_e^n varies for the different ionization cases.

III. RESULTS

According to the Keldysh parameter $\gamma = \sqrt{I_p/2U_p}$ [34,35], molecular ionization can be understood with different pictures. Here I_p is the ionization potential and U_p is the ponderomotive energy. When $\gamma \ll 1$, the electron experiences a field-dressed Coulomb potential, through which the electron has enough time to tunnel. Conversely, when $\gamma \gg 1$, the electron experiences a fast oscillation of the laser field and thus absorbs multiple photons and escapes from the nuclei. If the single-photon energy is larger than the ionization potential, the single-photon ionization will dominate. In the following, we look into the isotope effects on the one-photon ionization, multiphoton ionization, and tunneling ionization.

A. One-photon ionization

We used a 45-optical-cycle laser pulse with the frequency $\omega = 1.82$ a.u. ($\lambda = 25$ nm) and intensity 1.0×10^{14} W/cm^2 to irradiate H_2^+ and its isotopes. The JESs for H_2^+, D_2^+, and T_2^+ are shown in Figs. 1(a), 1(b), and 1(c), respectively. The slope of the JES in each panel clearly indicates that the electron and nuclei in the molecule share the single-photon energy. Though three panels present similar structures, the difference can be clearly seen by subtracting the JES of T_2^+ from that of H_2^+. Figure 1(d) presents the absolute difference $|\rho_{H_2^+} - \rho_{T_2^+}|$, which distinctly shows that the one-photon ionization of different isotopes results in different JESs.

The nuclear energy spectra can be obtained by integrating the JESs along the axis of the electron energy. According to the rule that the nuclear asymptotic kinetic energy is $E_N = 1/R$, where R is the internuclear distance for photon absorption and electron transition, the nuclear energy spectra can be transferred to the ionization probability as a function

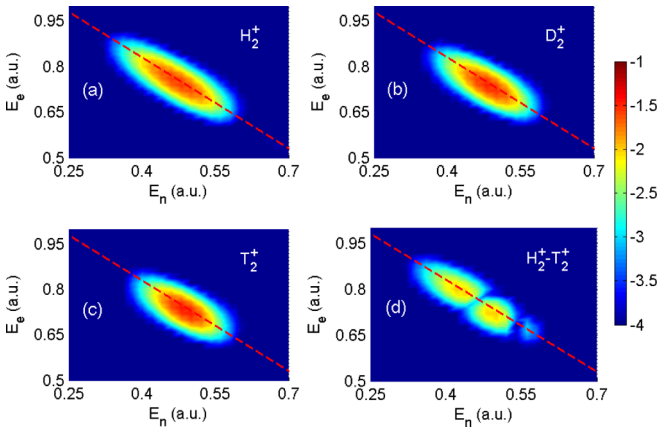

FIG. 1. The JESs for (a) H_2^+, (b) D_2^+, and (c) T_2^+ in the one-photon ionization process. (d) Difference of JESs for H_2^+ and T_2^+. The laser intensity is $I = 1.0 \times 10^{14}$ W/cm^2, the wavelength is 25 nm, and the energy resolutions are $\epsilon_e = 0.006$ and $\epsilon_\mu = 0.02$. The red dashed lines with the slope -1 indicate the energy sharing between the electron and nuclei.

of the internuclear distance, as shown in Fig. 2(b). Around the equilibrium internuclear distance, T_2^+ has a larger ionization probability than H_2^+. The two curves for T_2^+ and H_2^+ cross at $R = 1.81$ and 2.19 a.u. The mechanism charged for the physics shown in Fig. 2(b) can be retrospected from the initial nuclear wave-packet distribution, as presented in Fig. 2(a). Due to the different masses of the nuclei for H_2^+ and T_2^+, the nuclear wave packets of these two isotopes have different spatial distributions, though the Born-Oppenheimer potential curves are almost identical. Compared to T_2^+, the nuclear wave-packet distribution of H_2^+ is broader. Thus, around the equilibrium internuclear distance, the nuclear wave packet of T_2^+ has a larger proportion. For the ionization triggered

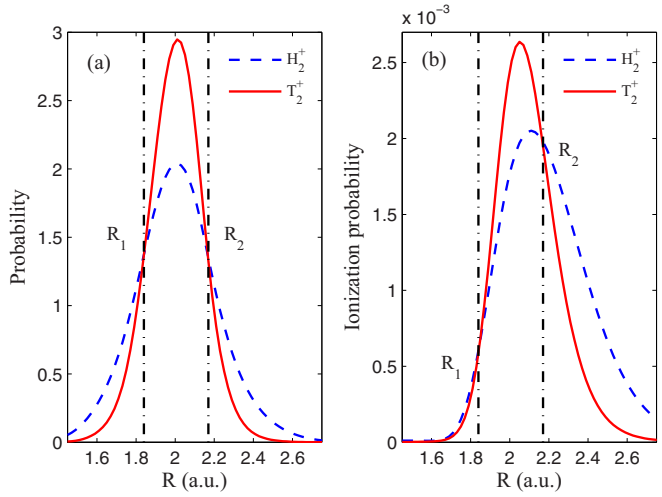

FIG. 2. (a) Initial nuclear wave-packet distributions of H_2^+ and T_2^+. (b) Ionization probability as a function of the internuclear distance. The vertical dash-dotted lines mark the locations of the two crossings (R_1 and R_2) of the two curves for H_2^+ and T_2^+. The locations of the crossings in (a) and (b) are same. The laser parameters are same as those in Fig. 1.

by the extreme ultraviolet pulse, the broad energy spectrum of the ultrashort pulse induces the single-photon ionization of the hydrogen molecular ion in a relative wide range of internuclear distance. The larger background of the nuclear wave packet of T_2^+ around $R = 2.0$ a.u. directly induces the larger ionization probability.

The locations of the crossing points in Figs. 2(a) and 2(b) are same, as indicated by the vertical dash-dotted lines. Based on this, the nuclear kinetic energy spectra of different isotopes can be used to extract the information of potential curves. As is well known, the potential around the equilibrium internuclear distance can be approximated as a harmonic potential [36] and different isotopic diatomic molecules have similar potential curves. Thus, the coefficient of elasticity of the potential curve can be extracted according to the following analysis. Using H_2^+ and T_2^+ as the prototypes, in experiment, we can obtain the crossing points of two nuclear energy spectra as R_1 and R_2, as shown in Fig. 2(b). The ground state of the harmonic potential is a Gaussian wave packet

$$\psi(R) \propto \sqrt{\alpha} e^{[-\alpha^2 (R-R_0)^2/2]}, \tag{7}$$

where $\alpha = \sqrt{M\omega_0}$ is a dimensionless parameter and $\omega_0 = \sqrt{K/M}$ is the harmonic vibrational angular frequency. Here K is the to-be-retrieved coefficient of elasticity of the potential. In addition, R_1 and R_2 are symmetric with respect to the equilibrium internuclear distance $R_0 = (R_1 + R_2)/2$ ($R_0 \approx 2.0$ a.u.). At the crossing point R_1 (or R_2), H_2^+ and T_2^+ have the same initial probability density, i.e., $\sqrt{\alpha_H} e^{[-\alpha_H^2 (R_1-R_0)^2/2]} = \sqrt{\alpha_T} e^{[-\alpha_T^2 (R_1-R_0)^2/2]}$. After some algebraic derivation, K can be written as

$$K = \left[\frac{2 \ln \sqrt[8]{M_H/M_T}}{(R_1 - R_0)^2 (\sqrt{M_H} - \sqrt{M_T})} \right]^2. \tag{8}$$

According to this equation, for H_2^+ and T_2^+ ions, the retrieved elastic constant K of the $1s\sigma_g$ potential curve is about 0.096 a.u. Thereby, we can further obtain the vibrational angular frequencies of H_2^+ and T_2^+, respectively, $\omega_H \approx 0.01$ a.u. and $\omega_T \approx 0.006$ a.u., which are almost identical to the data in Refs. [37,38]. Therefore, with the crossing point R_1 or R_2 from future experiments, one may extract information of molecular potential curves, which is a method of molecular imaging. In real experiments, the isotopic molecules may have different densities and thus the total ionization events in the same laser condition will be different. In this case, to get R_1 and R_2 correctly, one needs to normalize the photoelectron energy spectra by their own total ionization yields before making the comparison. Note that this method can only image the potential around the equilibrium internuclear distance and it does not work for the edge of the potential. Compared to traditional spectroscopic methods, this method does not need the frequency sweeping and is easy to apply.

B. Multiphoton ionization

When the single-photon energy is less than the ionization potential and the laser intensity is not very strong, multiphoton ionization takes place. Figure 3 shows the JESs for the multiphoton ionization of H_2^+, D_2^+, and T_2^+ irradiated by the 400-nm laser pulse. Visibly, the H_2^+ ion has a greater

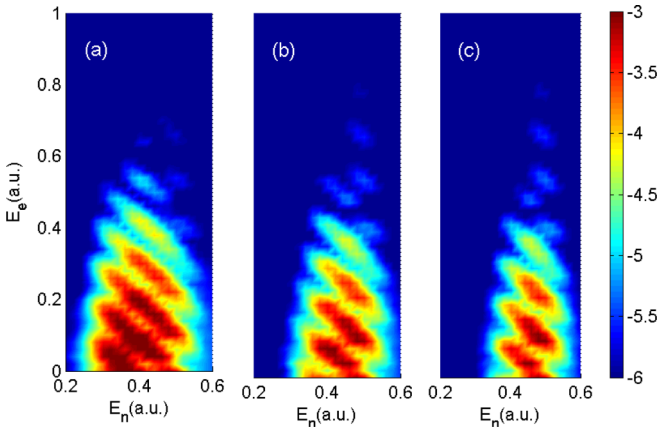

FIG. 3. The JESs for the multiphoton ionization of (a) H_2^+, (b) D_2^+, and (c) T_2^+. The laser pulse has an intensity $I = 1.0 \times 10^{14}$ W/cm^2, a wavelength of 400 nm, and a pulse duration of 12 optical periods with a CEP $\phi = 0$. The energy resolutions are $\epsilon_e = 0.004$ and $\epsilon_\mu = 0.02$.

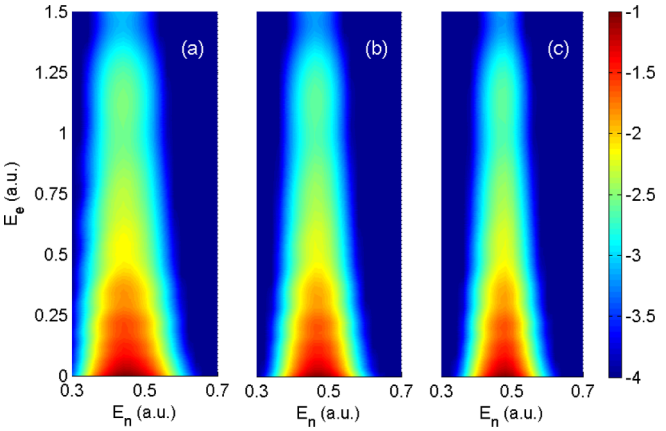

FIG. 4. The JESs for the tunneling ionization of (a) H_2^+, (b) D_2^+, and (c) T_2^+. The laser pulse has an intensity $I = 4.0 \times 10^{14}$ W/cm^2, a wavelength of 800 nm, and a pulse duration of two optical periods with a CEP $\phi = \pi/2$. The energy resolutions are $\epsilon_e = 0.01$ and $\epsilon_\mu = 0.02$.

ionization probability than the other two molecules. The multiple stripes with the same slope in each panel represent the above-threshold ionization (ATI) structure, demonstrating the absorption of multiple photons. While the electron energy spectra in three panels are similar, the nuclear energy spectra differ from each other. The nuclear energy spectrum of the ionization of H_2^+ has a broader distribution than that of T_2^+. Moreover, Fig. 3(a) shows a significantly larger proportion of the low-energy components than that in Fig. 3(c). These scenarios can be explained based on the initial distribution of the nuclear wave packet. For multiphoton ionization, the ionization is prone to occur at a larger internuclear distance where the ionization potential is smaller. The broad distribution of the initial nuclear wave packet of H_2^+ results in the broad distribution of the nuclear energy spectrum. The smaller ionization potential at a larger internuclear distance together with a larger background distribution of H_2^+ induces a much larger proportion of the low-nuclear-energy components.

C. Tunneling ionization

When the Keldysh parameter $\gamma \ll 1$, tunneling ionization happens. Figure 4 shows the JESs for the tunneling ionization of H_2^+, D_2^+, and T_2^+ ions. The laser pulse has a frequency $\omega = 0.057$ a.u. ($\lambda = 800$ nm), an intensity $I = 4.0 \times 10^{14}$ W/cm^2, and a pulse duration of two optical cycles with a CEP $\phi = \pi/2$. In this case, the energy sharing between the electron and nuclei is blurred and the R-independent horizontal peaks separated by the single-photon energy appear [39]. The horizontal ATI peaks are not conspicuous because of the ponderomotive energy shift and broad frequency spectrum of the ultrashort pulse. The three isotopes present similar JESs except that the nuclear energy spectrum of H_2^+ is still broader than those of two other isotopes. More importantly, the ionization probabilities for the three isotopes are distinct under the same laser radiation.

Figure 5 shows the ratios of the total ionization probability for the isotopes as a function of the laser intensity for different wavelengths. Among the three isotopes, H_2^+ has the largest ionization probability, and the ratio decreases monotonically and approaches one with the increase of the laser intensity in each panel. This scenario can be qualitatively explained based on the following two aspects. First, the ratios of the initial nuclear wave-packet distribution $|\psi(R)|_H^2/|\psi(R)|_T^2$ and $|\psi(R)|_D^2/|\psi(R)|_T^2$ are larger for larger R as $R > 2.2$. At a certain internuclear distance $R > 2.2$, the ionization rate of H_2^+ is larger than the other two isotopes. For tunneling ionization, the electron is released mainly from the range where the internuclear distance is large and the ionization potential is small. Second, in the tunneling range, if the laser intensity is weaker, the ionization events from larger internuclear distances have larger proportions in the whole

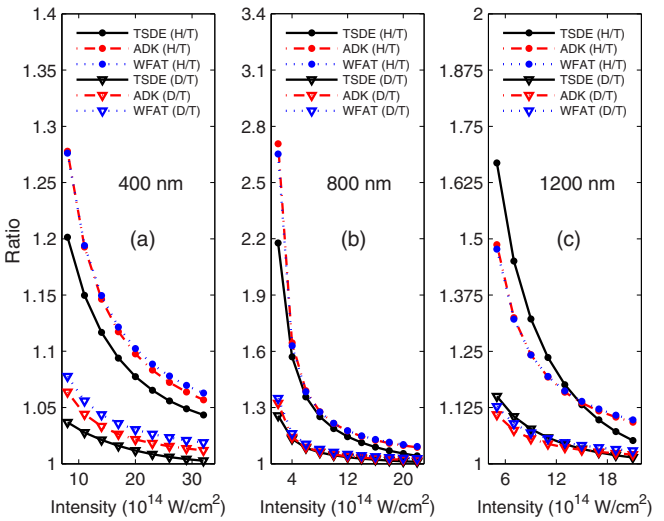

FIG. 5. Ratios of the ionization probabilities for H_2^+ and T_2^+ as well as D_2^+ and T_2^+ when the laser wavelength is (a) 400 nm, (b) 800 nm, and (c) 1200 nm. In each panel, the laser pulse duration has two optical cycles. For reference, the ratios calculated by the ADK theory and WFAT theory also are presented.

ionization probability. Thus, the ratios are larger if the driving laser intensity is weaker.

To see the importance of the nuclear movement during the ionization, we compare the ratios calculated by the TDSE, shown in Figs. 5(a)–5(c) for different laser wavelengths, with other theoretical analysis, in which the nuclear movement is not taken into account. For example, the R-dependent tunneling ionization rate $\Gamma(R)$ can be approximately described by the Ammosov-Delone-Krainov (ADK) theory [40,41],

$$\Gamma(R) = \frac{4[2I_p(R)]^{5/2}}{E} \exp\left(-\frac{2[2I_p(R)]^{3/2}}{3E}\right), \tag{9}$$

where $I_p(R)$ is the R-dependent ionization potential and E is the laser electric field. The total ionization probability can be calculated as

$$W = \int_0^\infty \Gamma(R)|\Psi(R)|^2 dR. \tag{10}$$

Alternatively, the ionization probability can be calculated using the weak-field asymptotic theory (WFAT) [24–26]

$$W \propto e^{\eta} L_\nu(-2\eta), \tag{11}$$

where $\eta = \frac{2\alpha_e^2(R_0)I_p(R_0)}{M\omega_0 E^2}$, $L_\nu(-2\eta)$ is a Laguerre polynomial with the dimensionless parameter η, and $\alpha_e(R_0)$ is the first derivative of the electron energy at the equilibrium molecular bond length R_0. One may clearly see that the ADK theory and WFAT results share quite similar tendencies with the TDSE simulation results on the whole. The larger ionization probability of H_2^+ is mainly due to the broad distribution of the initial nuclear wave packet. In detail, the distinct disagreement for 400 nm between the TDSE and ADK or WFAT may be due to the nonadiabatic tunneling processes. The good agreement appears for 800 nm when the laser intensity exceeds 4.0×10^{14} W/cm^2. For the case of 1200 nm, the results of the TDSE do not match those expected for the ADK or WFAT as well as for the case of 800 nm.

To see in what sense the ADK theory and WFAT can describe the ionization reasonably well, we look into the ionization for the laser pulse with different pulse durations. Figure 6 shows the ratios of the ionization probabilities for different isotopes when the 800-nm laser pulse durations are different. The ADK theory and WFAT results are also presented as reference. When the pulse duration is longer and longer, the ratios calculated by TDSE simulations deviate from the ADK theory and WFAT results more severely, which means that the ADK theory and WFAT do not work well. The difference between TDSE simulations and the analytical methods originates fundamentally from the nuclear movement. When the laser pulse duration is comparable to the timescale for nuclear movement, which is about 10 fs, the fixed-nuclei approximation does not hold any longer. For H_2^+, the lighter nucleus moves faster and approaches the larger internuclear distance quicker. Thus, H_2^+ has a much larger population in the area of the relatively large internuclear distance than D_2^+, which leads to even larger ratios of the ionization probabilities of H_2^+ and T_2^+, as presented in Fig. 6(a).

For longer wavelengths, the interaction is closer to the adiabatic ionization regime and thus the ADK theory and WFAT work better. However, the pulse having longer wavelengths

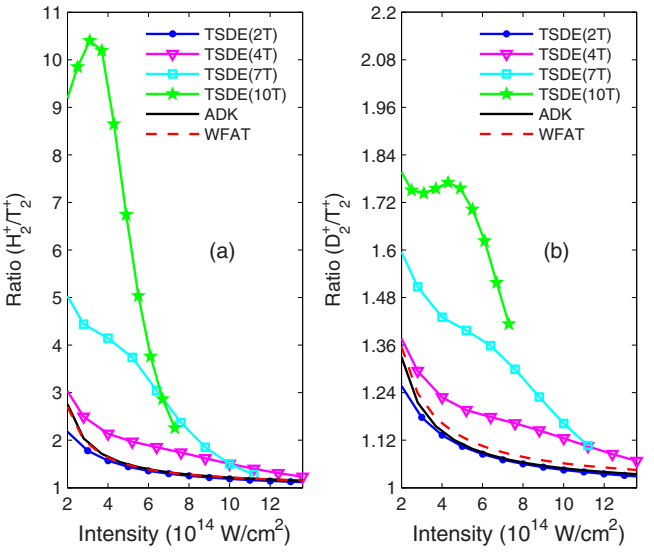

FIG. 6. Ratios of the ionization probabilities for (a) H_2^+ and T_2^+ and (b) D_2^+ and T_2^+ when the driving laser field has different optical cycles. The ratios predicted by the ADK theory and the WFAT are shown by the black solid and red dashed curves, respectively. The laser wavelength is 800 nm. For the lines using 7T and 10T, the lines are truncated when the ionization depletion is important.

also offers a longer time for nuclear relaxation. As shown in Fig. 7, when the laser field is 800 or 1200 nm with the same intensity, it is easier to populate the 1200-nm laser with more excited vibrational states, leading to faster nuclear movement. Here the time-dependent probabilities of vibrational states are obtained by projecting the time-dependent molecular wave function to each vibrational eigenstate. Therefore, we believe

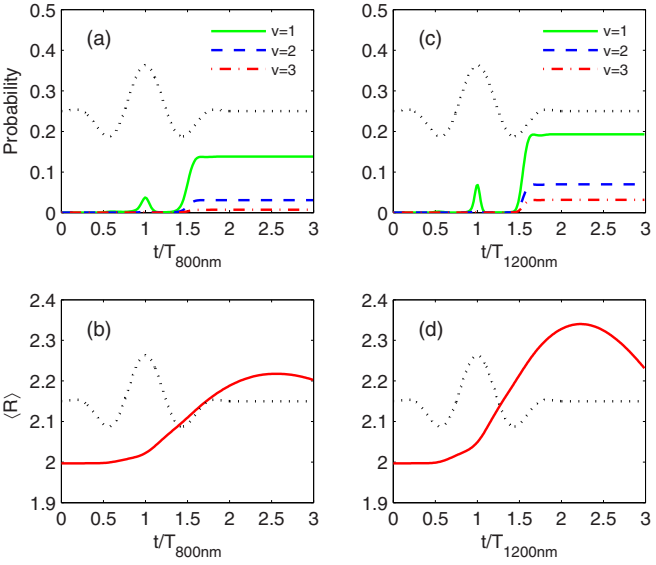

FIG. 7. Time-evolved probabilities of different vibrational states when the laser wavelength is (a) 800 nm and (c) 1200 nm. Also shown is the time-dependent internuclear distance of H_2^+ when the laser wavelength is (b) 800 nm and (d) 1200 nm. The black dotted curves represent the two-cycle laser electric field.

that the ADK theory and WFAT work better in the tunneling regime but with a sufficiently short pulse duration.

IV. CONCLUSION

Our study has shown that H_2^+, D_2^+, and T_2^+ ions have clearly different behaviors in different ionization regimes. The ionization enhancement of H_2^+ in the tunneling regime is not necessarily due to the nuclear movement. In single-photon ionization, the crossing points R_1 and R_2 shown in Fig. 2(b) are the same as those in Fig. 2(a), which confirms that the nuclear movement during the one-photon ionization is negligible and thus justifies the fixed-nuclei approximation in the one-photon ionization. In tunneling ionization, the overall agreement among the ADK theory, WFAT, and TDSE results also supports the negligible nuclear movement during the ionization for a short pulse duration. The multiphoton and tunneling ionization enhancement of H_2^+ is fundamentally due to the broader spatial distribution of the nuclear wave packet, which is further determined by nuclear mass.

To summarize, the ionization of H_2^+ and its isotopic molecules in strong laser fields has been studied using the time-dependent Schrödinger equation. Due to the different nuclear masses of H_2^+, D_2^+, and T_2^+, the initial nuclear wave-packet distributions are different. For H_2^+, the nuclear distribution on the potential curve with a larger internuclear distance and smaller ionization potential has larger proportions, which makes H_2^+ have a larger tunneling ionization probability than its heavier isotopic molecules. The nuclear energy spectra from the single-photon ionization of isotopic molecules can be used to extract the elastic constants of molecular potential curves, which is a different perspective to image molecules.

ACKNOWLEDGMENTS

This work was supported by National Key R&D Program of China (Grant No. 2018YFA0404802), Innovation Program of Shanghai Municipal Education Commission (Grant No. 2017-01-07-00-02-E00034), National Natural Science Foundation of China (Grants No. 11574205, No. 11721091, and No. 91850203), Shanghai Shuguang Project (No. 17SG10), the Zhiyuan Scholar Program (Grant No. ZIRC2017-04). Simulations were performed on the π supercomputer at Shanghai Jiao Tong University.

[1] J. H. Posthumus, Rep. Prog. Phys. **67**, 623 (2004).
[2] M. R. Miller, Y. Xia, A. Becker, and A. Jaroń-Becker, Optica **3**, 259 (2016).
[3] H. Ibrahim, C. Lefebvre, A. D. Bandrauk, A. Staudte, and F. Légaré, J. Phys. B **51**, 042002 (2018).
[4] A. Giusti-Suzor, F. H. Mies, L. F. DiMauro, E. Charron, and B. Yang, J. Phys. B **28**, 309 (1995).
[5] M. Protopapas, C. H. Keitel, and P. L. Knight, Rep. Prog. Phys. **60**, 389 (1997).
[6] P. H. Bucksbaum, A. Zavriyev, H. G. Muller, and D. W. Schumacher, Phys. Rev. Lett. **64**, 1883 (1990).
[7] L. J. Frasinski, J. H. Posthumus, J. Plumridge, K. Codling, P. F. Taday, and A. J. Langley, Phys. Rev. Lett. **83**, 3625 (1999).
[8] A. Giusti-Suzor, X. He, O. Atabek, and F. H. Mies, Phys. Rev. Lett. **64**, 515 (1990).
[9] P. Lu, J. Wang, H. Li, K. Lin, X. Gong, Q. Song, Q. Ji, W. Zhang, J. Ma, H. Li, H. Zeng, F. He, and J. Wu, Proc. Natl. Acad. Sci. USA **115**, 2049 (2018).
[10] D. Ray, F. He, S. De, W. Cao, H. Mashiko, P. Ranitovic, K. P. Singh, I. Znakovskaya, U. Thumm, G. G. Paulus, M. F. Kling, I. V. Litvinyuk, and C. L. Cocke, Phys. Rev. Lett. **103**, 223201 (2009).
[11] H. Xu, Z. C. Li, F. He, X. Wang, A. Atia-Tul-Noor, D. Kielpinski, R. T. Sang, and I. V. Litvinyuk, Nat. Commun. **8**, 15849 (2017)
[12] J. J. Hua and B. D. Esry, J. Phys. B **42**, 085601 (2009).
[13] T. Ergler, A. Rudenko, B. Feuerstein, K. Zrost, C. D. Schröter, R. Moshammer, and J. Ullrich, Phys. Rev. Lett. **97**, 193001 (2006).
[14] J. Zhang, G. Q. He, and F. He, Mol. Phys. **112**, 1929 (2014).
[15] M. Lein, Phys. Rev. Lett. **94**, 053004 (2005).
[16] C. C. Chiril and M. Lein, J. Phys. B **39**, S437 (2006).
[17] P. Lan, M. Ruhmann, L. He, C. Zhai, F. Wang, X. Zhu, Q. Zhang, Y. Zhou, M. Li, M. Lein, and P. Lu, Phys. Rev. Lett. **119**, 033201 (2017).
[18] Y.-N. Yang, L. Xu, and F. He, Phys. Rev. A **98**, 053409 (2018).
[19] X.-B. Bian and A. D. Bandrauk, Phys. Rev. Lett. **113**, 193901 (2014).
[20] M. Lara-Astiaso, R. E. F. Silva, A. Gubaydullin, P. Rivière, C. Meier, and F. Martín, Phys. Rev. Lett. **117**, 093003 (2016).
[21] X. M. Tong, Z. X. Zhao, and C. D. Lin, Phys. Rev. A **66**, 033402 (2002).
[22] S.-F. Zhao, C. Jin, A.-T. Le, T. F. Jiang, and C. D. Lin, Phys. Rev. A **81**, 033423 (2010).
[23] O. I. Tolstikhin, T. Morishita, and L. B. Madsen, Phys. Rev. A **84**, 053423 (2011).
[24] O. I. Tolstikhin, H. J. Wörner, and T. Morishita, Phys. Rev. A **87**, 041401(R) (2013).
[25] O. I. Tolstikhin and L. B. Madsen, Phys. Rev. Lett. **111**, 153003 (2013).
[26] O. I. Tolstikhin and T. Morishita, Phys. Rev. A **95**, 033410 (2017).
[27] X. Wang, H. Xu, A. Atia-Tul-Noor, B. T. Hu, D. Kielpinski, R. T. Sang, and I. V. Litvinyuk, Phys. Rev. Lett. **117**, 083003 (2016).
[28] B. Feuerstein and U. Thumm, Phys. Rev. A **67**, 043405 (2003).
[29] R. Kosloff and H. Tal-Ezer, Chem. Phys. Lett. **127**, 223 (1986).
[30] W. H. Press, S. A. Teukolsky, W. T. Vetterling, and B. F. Flannery, in *Numerical Recipes* (Cambridge University Press, Cambridge, 1992), p. 842.
[31] F. Catoire and H. Bachau, Phys. Rev. A **85**, 023422 (2012).

[32] R. E. F. Silva, F. Catoire, P. Rivière, H. Bachau, and F. Martín, Phys. Rev. Lett. **110**, 113001 (2013).
[33] F. Catoire, R. E. F. Silva, P. Rivière, H. Bachau, and F. Martín, Phys. Rev. A **89**, 023415 (2014).
[34] L. V. Keldysh, Zh. Eksp. Teor. Fiz. **47**, 1945 (1965) [Sov. Phys. JETP **20**, 1307 (1965)].
[35] M. Y. Ivanov, M. Spanner, and O. Smirnova, J. Mod. Opt. **52**, 165 (2005).
[36] W. Demtröder, in *Molecular Physics: Theoretical Principles and Experimental Methods* (Wiley-VCH, Weinheim, 2005), p. 87.
[37] K. P. Huber and G. Herzberg, in *Molecular Spectra and Molecular Structure IV: Constants of Diatomic Molecules* (Van Nostrand-Reinhold, New York, 1978), p. 274.
[38] J. E. Pollard, D. J. Trevor, J. E. Reutt, Y. T. Lee, and D. A. Shirley, J. Chem. Phys. **77**, 34 (1982).
[39] K. Liu, P. Lan, C. Huang, Q. Zhang, and P. Lu, Phys. Rev. A **89**, 053423 (2014).
[40] M. V. Ammosov, N. B. Delone, and P. V. Krainov, Zh. Eksp. Teor. Fiz. **91**, 2008 (1986) [Sov. Phys. JETP **64**, 1191 (1986)].
[41] D. Bauer and P. Mulser, Phys. Rev. A **59**, 569 (1999).